Stress imparted by the great 2004 Sumatra earthquake shut down transforms and activated rifts up to 400 km away in the Andaman Sea

Volkan Sevilgen[a,1], Ross S. Stein[b], and Fred F. Pollitz[b]

[a]Seismicity.net, 490 Laurel Street, Suite 10, San Carlos, CA 94070; and [b]U.S. Geological Survey, 345 Middlefield Road, MS 977, Menlo Park, CA 94025

Edited by* Peter M. Shearer, University of California, San Diego, La Jolla, CA, and approved July 31, 2012 (received for review May 24, 2012)

The origin and prevalence of triggered seismicity and remote aftershocks are under debate. As a result, they have been excluded from probabilistic seismic hazard assessment and aftershock hazard notices. The 2004 $M = 9.2$ Sumatra earthquake altered seismicity in the Andaman backarc rift-transform system. Here we show that over a 300-km-long largely transform section of the backarc, $M \geq 4.5$ earthquakes stopped for five years, and over a 750-km-long backarc section, the rate of transform events dropped by two-thirds, while the rate of rift events increased eightfold. We compute the propagating dynamic stress wavefield and find the peak dynamic Coulomb stress is similar on the rifts and transforms. Long-period dynamic stress amplitudes, which are thought to promote dynamic failure, are higher on the transforms than on the rifts, opposite to the observations. In contrast to the dynamic stress, we calculate that the mainshock brought the transform segments approximately 0.2 bar (0.02 MPa) farther from static Coulomb failure and the rift segments approximately 0.2 bar closer to static failure, consistent with the seismic observations. This accord means that changes in seismicity rate are sufficiently predictable to be included in post-mainshock hazard evaluations.

Coulomb stress transfer | great earthquakes | seismicity rate changes

Whether aftershocks and subsequent mainshocks are triggered by the small but permanent static stress changes or the larger but oscillatory dynamic stress changes is unresolved (1–8). Partly in consequence, aftershocks have been omitted from probabilistic seismic hazard assessment even though the ground motion and damage they cause can sometimes exceed that of the mainshock. By virtue of its size, the 26 December 2004 $M = 9.2$ Sumatra earthquake (9–11) permits study of how seismicity far from the rupture is promoted and inhibited by a mainshock. The earthquake struck along the Sunda trench, where the Indian-Australian plate undergoes oblique subduction (Fig. 1). At the northern portion of the rupture zone, the Andaman backarc rift-transform system lies 200–400 km from the megathrust (12–14) (Fig. 1). This separation from the megathrust means that stress transferred to the backarc by the megathrust is insensitive to the unknown details of the coseismic slip distribution and geometry. But because of the size of the mainshock, the calculated static stress imparted to the Andaman backarc exceeds 0.2 bar (0.02 MPa), about twice the commonly observed threshold seen to influence seismicity (2, 15), making the Sumatra-Andaman event an ideal test case of long-distance earthquake triggering and inhibition. At magnitudes up to 6.2 backarc, earthquakes are also large enough to cause damage if they struck in many regions of the world, and so understanding what controls them matters to hazard assessment.

Seismicity Observations

The National Earthquake Information Center (NEIC) and the Global CMT (gCMT) catalogs permit us to compare the 26-y record of preceding or 'background' seismicity to the 6 y of aftershocks and post-mainshock seismicity, which reveals a 330-km-long dominantly-transform section of the Andaman backarc system that is devoid of earthquakes during the first 5 y after the mainshock (Fig. 2 *A* and *B*). The magnitude of completeness, Mc, is 4.5 for NEIC (Fig. S1) and 5.2 for gCMT, and so we count only earthquakes above these thresholds. The post-mainshock shutdown of NEIC earthquakes (16) is evident in map view (Fig. 2 *A* and *B*) and in time series (Fig. 3), where it is marked as Box N. It is also evident after aftershocks and foreshocks are removed by declustering (17) (Figs. S2 and S3 *A* and *B*). The next largest temporal gap in the full or declustered catalog is 3.5 y. It is unlikely that the observed gap is a detection artifact, because Box S of similar dimension along the backarc (Fig. 2) exhibits an abrupt rate increase at the time of the $M = 9.2$ event in the full catalog (Fig. 3), or no rate change in the declustered catalog (Fig. S3*B*).

Along a longer 750-km-long section of the back-arc system that includes both rifts and transforms, earthquake focal mechanisms changed after the 2004 mainshock, as first reported by Andrade and Rajendran (2011) (18). Whereas more than half of the 28 events were strike-slip before the mainshock (Fig. 4*A*), only one of the 21 events was afterwards (Fig. 4*B*), an 800% gain in the rate of normal events and a 66% drop in the rate of strike-slip events (Table S1). Comparison of Fig. 4 *A* and *B* indicates that the transform segments became seismically inactive after the 2004 mainshock. If strike-slip or normal mechanisms could occur with equal likelihood, roughly as in the pre-mainshock period (54/46%), the probability of drawing 20 normal events out of 21 is 0.19%. The focal mechanism change is also evident in a space-time plot (Fig. S4*A*). Thus, we observe earthquake activation along the rifts and inhibition along the transforms after the 2004 mainshock. This could be a product of the dynamic or static stresses.

Coulomb Stress Transfer

To calculate the Coulomb stress transmitted to the Andaman backarc system, we treat the transforms as vertical right-lateral faults, and the rifts as 45°dipping normal faults, based on the geometry of other well-imaged oceanic transform-rift systems (19, 20). We then impose the 2004 coseismic slip in an elastic halfspace for the static stress, or a spherically layered earth for the dynamic stress, and calculate the Coulomb stress change. After 1,000 s the dynamic stresses closely resemble the static stresses calculated in a halfspace. The Coulomb stress change $\Delta CFF = \Delta\tau + \mu'\Delta\sigma$, where τ is the shear stress on the fault (positive in the direction of slip), σ is the normal stress (positive for unclamping), and μ' is the apparent friction coefficient. Failure is promoted if ΔCFF is positive, and inhibited if negative. Thus both increased

Author contributions: V.S. and R.S. designed and conducted the study; F.P. contributed to the dynamic Coulomb model.

The authors declare no conflict of interest.

*This Direct Submission article had a prearranged editor.

Freely available online through the PNAS open access option.

[1]To whom correspondence should be addressed. E-mail: vsevilgen@usgs.gov.

This article contains supporting information online at www.pnas.org/lookup/suppl/doi:10.1073/pnas.1208799109/-/DCSupplemental.

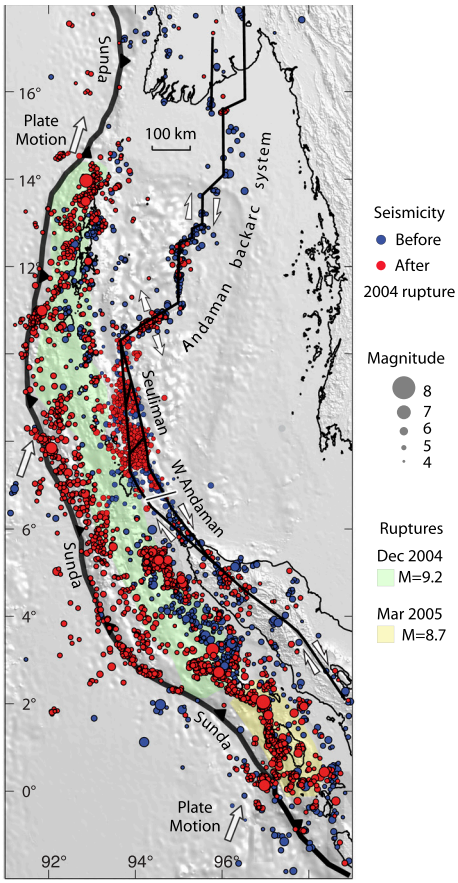

Fig. 1. Tectonic setting of the 2004 Sumatra earthquake. $M \geq 4$ seismicity during the 30 y before the mainshock is blue, and during 5 y afterwards is red; all relocated earthquakes (16) are shown, including those below the completeness level. The Indian-Australian plate subducts obliquely at approximately 38 mm/y, the West Andaman and Seuliman transforms slip at approximately 20 mm/y each, the Sumatra transform slips at approximately 23 mm/y (40), and the Andaman rift-transform backarc system has opened at 38 mm/y since 4–11 Ma (35). Plate motion is relative to Eurasia. Black lines give the back-arc interpreted from bathymetric surveys (12, 14) (and GEBCO_08, http://www.gebco.net), earthquakes (16), and relocated gCMT focal mechanisms (Fig. S6).

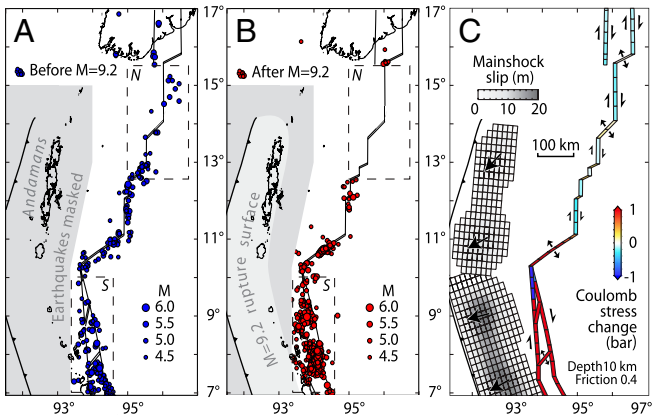

Fig. 2. Change in back-arc seismicity after 2004 and comparison with static stress transfer. (*A*–*B*) Relocated $M \geq 4.5$ seismicity (16) for 1 Jan 1975—31 Oct 2009. Straight single lines represent right-lateral transforms, double lines are rifts. Earthquakes near the 2004 rupture surface are masked. (*C*) Coulomb stress imparted by the mainshock with rake shown by black arrows (7) to the interpreted back-arc fault system (with sense of slip given by gray arrows).

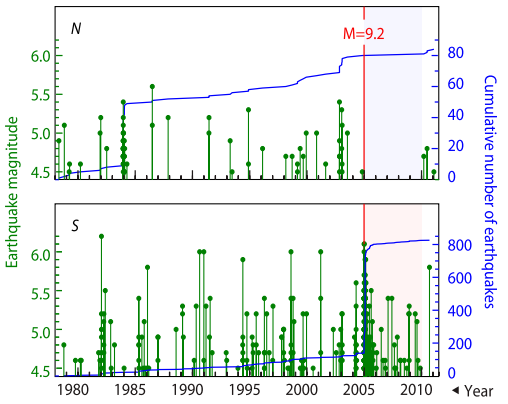

Fig. 3. Time series of NEIC $M \geq 4.5$ seismicity for depths $\leq$60 km. Green dots with stems are individual events; blue lines give the cumulative number. Color shaded areas indicate the post-mainshock analysis period. Time series for the declustered catalog are shown in Fig. S3.

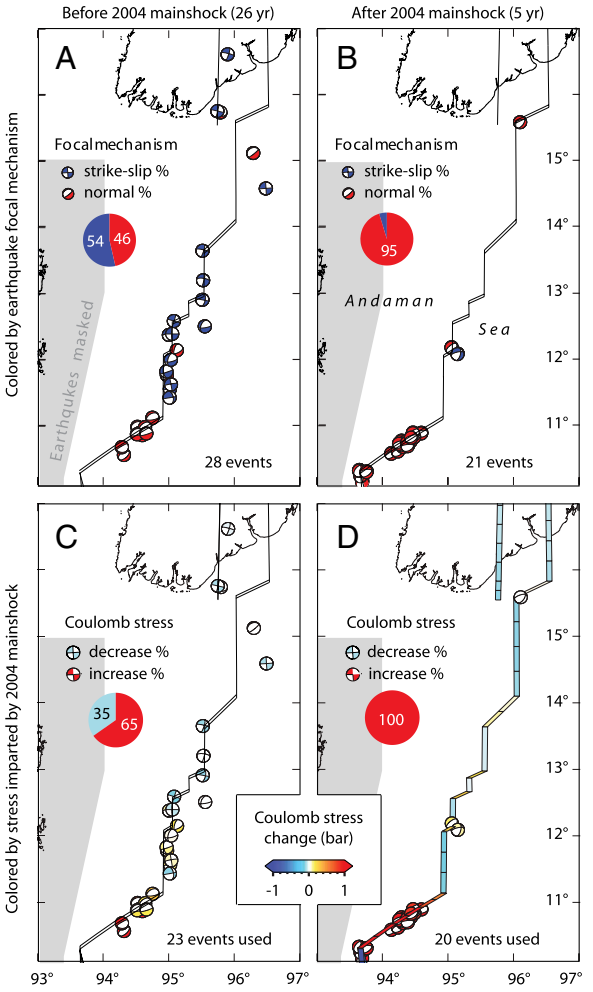

Fig. 4. Shutdown of transform events and activation of rift events. (*A*–*B*) $M \geq 5.2$ earthquakes colored by their rake (blue $\leq -135° <$ red). (*C*–*D*) Earthquakes colored by the stress change imparted by the 2004 mainshock, using the (9) source and friction = 0.4; mechanisms with negligible stress changes ($\Delta CFF < |0.05|$ bar) are excluded from the pie charts. Receiver faults are taken to be the most-northerly striking nodal planes of each pair. (*A* and *C*) Earthquakes before the 2004 mainshock; (*B* and *D*) earthquakes afterwards. The Coulomb model in (*D*) is judged relative to the control in (*C*) following (30), with a 54% improvement in fit (Table S1). A similar analysis of the earthquakes in Box S of Fig. 2 is given in Fig. S7.

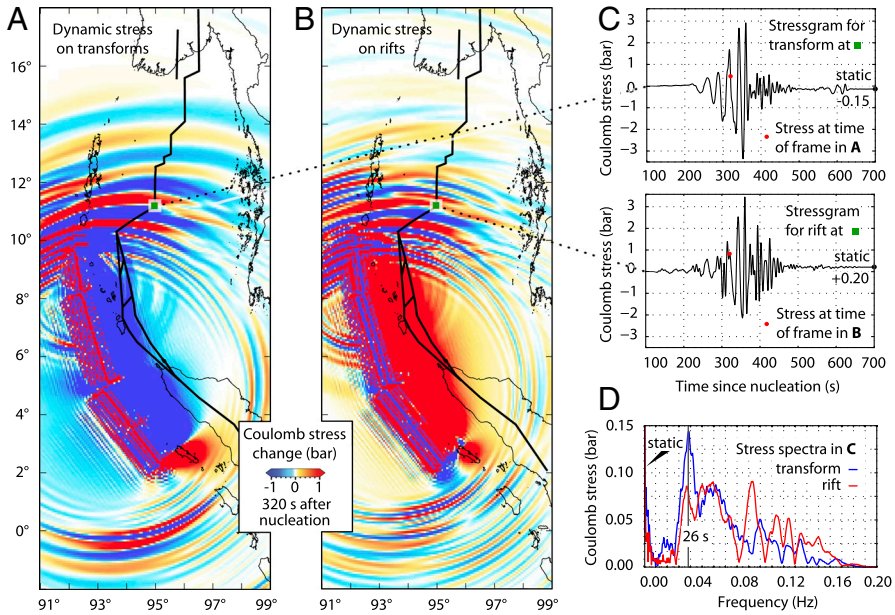

Fig. 5. Dynamic Coulomb stress 320 s after nucleation, resolved on N-striking vertical right-lateral faults typical of the transform sections (*A*), and on N45 °E-striking 45°dipping normal faults typical of the rift sections (*B*). (*C*) Stressgrams at a rift-transform junction; the *p* wave arrival is seen at 118 s, and the peak positive pulses have approximately 10-s durations. (*D*) Spectrum shows the static (zero frequency) stress changes, and the much higher stress at approximately 26 s on the transforms in comparison to the rifts.

shear and unclamping of faults are taken to promote failure, with the influence of unclamping controlled by friction.

Dynamic Stress

We first seek to explain these observations by the dynamic Coulomb stress carried by the surface waves. An isotropic PREM was used as the spherically-symmetric reference Earth structure (21). Implementation of the direct Green's function method (22, 23) involved all spherical harmonic degrees from 0–3000, and discretization of the finite fault plane into approximately 35 km^2 patches sufficient to sample the wavefield with at least 10 points per wavelength. We use 6 × 6 km grid spacing, low-pass filtered with a corner period of 10 s, and calculate the stress at 10 km depth (for comparison, the depth of post-mainshock rift events is 13 ± 7 km). For simplicity, we use the Banerjee et al. (10) source model composed of eight rectangular surfaces for the dynamic stress calculation. The rupture propagates northward at 2.8 km/s based on (24), activating 6,000 slip patches on these eight surfaces in succession. We resolve the resulting stress on transforms and on rifts.

Movie S1 reveals the pronounced northward directivity that some studies infer is required to promote dynamic triggering (4, 25); the strongest Coulomb stress waves sweep past the transform section of the backarc 320–370 s after nucleation (Fig. 5 and Movie S1). The stressgrams in Figs. 5 and 6, and Movie S1 reveal the dynamic stress changes generated by the full array of regional seismic phases (P, S, L, R, and the reflected phases). The peak dynamic Coulomb stresses occur during the passage of the Love

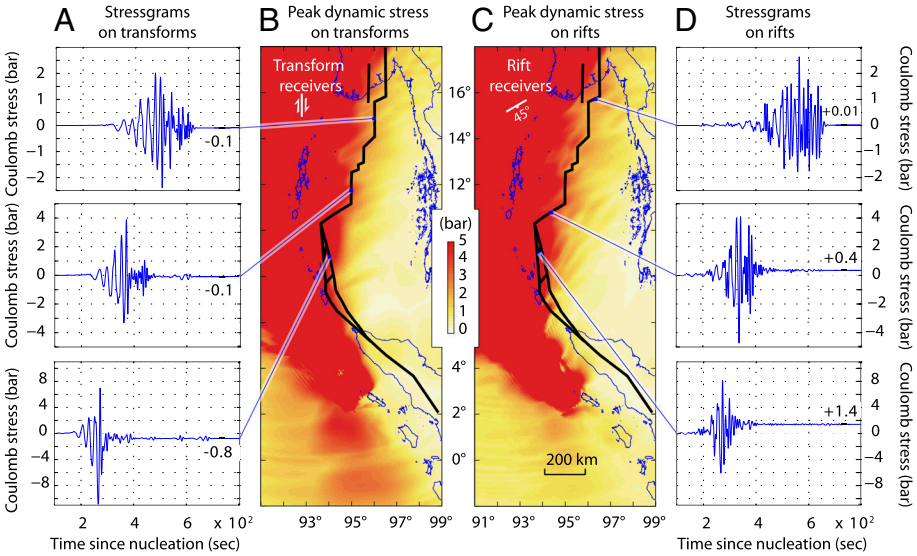

Fig. 6. Peak dynamic stress (the most positive value attained anytime during 1000 s minus the static stress) and stressgrams resolved on transforms (*A–B*), and rifts (*C–D*), at 10 km depth for friction of 0.2. The peak dynamic stress along the backarc is similar (within 0.25 bar) on transforms and rifts. The stress amplitude decays and the duration grows toward the north, in the directivity direction. Note that the stress scale for the stressgrams changes from south to north.

wave train, similar to that found for triggering of global microearthquakes (7).

We find that the peak dynamic stress is similar on rifts and transforms over 618 °N lat. (Fig. 6). The peak stress on transform faults exceeds 2 bar north of 12.5 °N, where transform events halted. Although some studies conclude that long period (>30 s) energy is necessary for dynamic triggering (4, 25), long-period stress amplitudes are higher on the transforms than on rifts (Figs. 5*D* and 6), opposite to the observed transform shutdown and rift activation. Thus, as best we can infer, the calculated dynamic stress cannot explain the observations. The first backarc events occur 80 min after the mainshock, and Omori decay begins 3 h after the mainshock (Fig. 7), and so detection is likely complete from 3 h onward. Thus it is possible that $M \geq 4.5$ earthquakes struck undetected along both rifts and transforms up to 3 h of the passage of the stress waves, but not later.

Static Stress

The static Coulomb stress change is calculated using the Chlieh et al. (9) source in Fig. 2*C* for fault friction of 0.4. The stress change as a function of fault friction is shown in Fig. 8 for the same source (9), and in Fig. S5 for the alternative source (10). The static stress rises on the rifts and drops along the transforms in both models, matching the observations for friction of 0.2–0.4. Oceanic and mature continental transforms generally exhibit evidence for low apparent friction (26, 27), most likely due to their geometrical continuity and thick fault gouge. Oceanic and volcanic rifts are also found to possess friction of 0.01–0.40 (28, 29), probably due to high temperature, high pore pressure, or a thin crust. Thus, the assumption of low friction appears warranted, but to reduce bias toward the expectation of low friction, we nevertheless use friction of 0.4.

We also calculated the static stress imparted to the earthquake nodal planes at their hypocentral depths (Fig. 4 *C* and *D*). Although the shear stress change on each pair of nodal planes is the same, the normal stress change is not. Thus, except for the special case of frictionless faults, the Coulomb stress change on the two nodal planes is different. Because of the NNE strike of the backarc, we select the most northerly-striking plane of each pair as the more likely fault, and find that all 21 post-2004 mechanisms were brought closer to Coulomb failure by the 2004 mainshock. For the control population (30), we calculate the percentage of pre-2004 mechanisms brought closer to failure by the 2004 mainshock, again selecting the most northerly-striking planes, finding 65% were positive (Table S1). If two out of three focal mechanisms are promoted at random as in the pre-mainshock control period, the probability that all 20 shocks would be promoted after the mainshock is 0.03%. For this test, we drew 100,000 sets of 20 earthquakes from a population in which 66% of the events are promoted, and calculated the chance that all

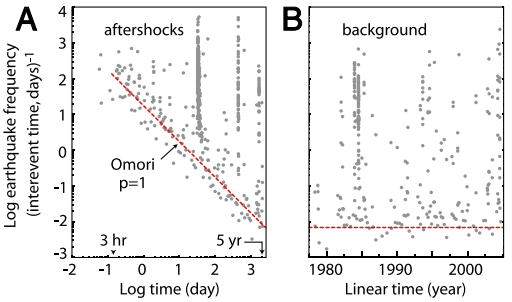

Fig. 7. Aftershock decay along the Andaman backarc-transform system, using $M \geq 4.7$ NEIC earthquakes from the unmasked area of Fig. 2. (*A*) These remote aftershocks decay with $p = 1$ starting 3 h after the 2004 mainshock, with excursions after the largest aftershocks; the plot ends on 12 Jul 2011. (*B*) Judging from the foregoing 32-y period, the background baseline rate is 10^{-2} y^{-1}, suggesting that the aftershock decay ended by mid- to late-2011.

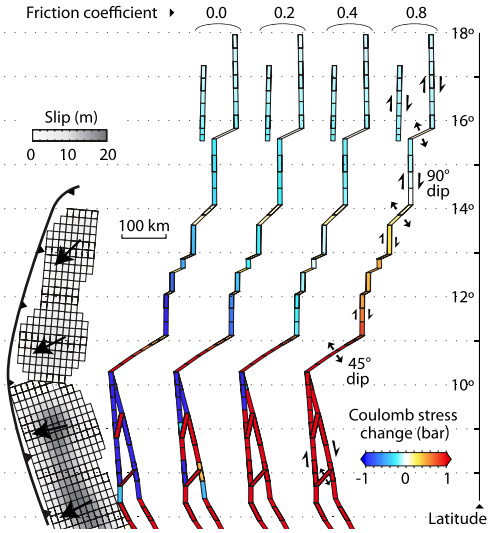

Fig. 8. Coulomb stress at 10 km depth as a function of friction on the backarc system, using the 400-patch (9) mainshock source. Black vectors on the source give fault slip azimuths. Transforms are assumed to be vertical and rifts dip 45° southeast. Results are little changed for 15 km depth or for 60°-dipping rift normal faults. Fig. S5 shows similar results for the 8-patch (10) source.

20 shocks will be promoted after the mainshock. By comparison, a previous analysis (31) resolved only a subtle 5-y change in observed focal mechanisms in the stress shadows of global $M \geq 7$ mainshocks.

Discussion and Conclusions

We argue that the $M = 9.2$ Sumatra earthquake caused a 5-y shutdown of moderate to large earthquakes along the transform system, and a corresponding change in focal mechanisms. The apparent return of seismicity after 5 y (Fig. 3*A*, *Top*) mirrors the aftershock duration for the backarc-transform system (Fig. 7): Aftershock frequency decays with inverse time, reaching the pre-mainshock background rate about 5 y after the 2004 mainshock. Thus, the duration of the seismicity rate drop in the stress shadow resembles the duration of the seismicity rate gain in the stress trigger zones.

We consider the results we report for the Sumatra earthquake to be more complete than but consistent with those from other large shocks. The 1992 $M = 7.3$ Landers earthquake produced a strong seismicity shutdown in its stress shadow up to 35 km from the source, but no focal mechanism change (32). The 2011 $M = 9.0$ Tohoku-oki earthquake produced a focal mechanism change inland of the megathrust—from reverse events before the mainshock to normal mechanisms afterwards—consistent with static stress change, but exhibited a very limited seismicity shutdown (33). Not only does the post-Sumatra period span the full 5-y aftershock decay, its aftershock observations exhibit all of the distinguishing features of static stress changes.

Cattin et al. (34) also calculated the static stress transferred to the backarc by the 2004 mainshock, finding a Coulomb stress increase on the transforms and a decrease on the rifts at 11°–15 °N lat., opposite to our results. Although we use the same source (9), our interpretations of the backarc faults differ. What we regard as a N-S transform, they view as a set of 15-km-long en echelon NW-striking normal faults. But such short normal faults could not accommodate the 150 km of right-lateral displacement associated with the opening of the Andaman Basin (35). We consider such normal faults as a secondary features often seen near transforms. We base our inference on 376 focal mechanisms (they used 83), most of which are strike-slip along the transform (Fig. 4*A*). As a result of their fault interpretation, they infer fault friction >0.5,

while we infer 0.2–0.4, consistent with studies of the other seafloor spreading centers. Finally, Cattin et al. (34) consider 2 y of post-mainshock events (36), while we use 5–7 y of relocated events (16); the longer period permits identification of the seismicity rate drop along the transforms.

The remote changes in seismicity rate have implications for seismic hazards. If a mainshock can promote or inhibit earthquakes far from the fault rupture, it changes not just the local but also the regional risk of subsequent earthquake damage. This is important because damage to buildings can be more strongly influenced by moderate nearby earthquakes than by shaking from the large distant mainshock that triggered those remote shocks. For example, a $M = 6$ event 10 km from a twostory house (typical resonant period of 0.2 s) produces the same spectral acceleration as a $M = 9$ earthquake 100 km away; a $M = 6$ shock 10 km from a 30-story building (3 s period) produces the same spectral acceleration as a $M = 9$ earthquake 500 km away (37). Nowhere was this clearer than when a $M = 6.3$ aftershock of the 4 September 2010 $M = 7.1$ Darfield, New Zealand, earthquake struck 45 km away in Christchurch five months later, tripling the insured losses (38, 39) and causing 181 deaths.

We thus offer this study and the calculation of the full dynamic animations as a contribution to the ongoing debate about to what extent, and to what distance, static or dynamic stresses trigger earthquakes (1–8). We find that the static stress imparted by the 2004 mainshock best explains the observed changes in focal mechanisms and seismicity rate.

ACKNOWLEDGMENTS. We thank Shinji Toda, David Hill, Tom Parsons, Andy Michael, and Jian Lin for discussion and sage advice; Jeremy Pesicek for generously sharing his catalog with us before publication; and David Shelly, Ruth Harris, and Jeanne Hardebeck for perceptive reviews. V.S. works under contract at the U.S. Geological Survey.

1. Kilb D (2003) A strong correlation between induced peak dynamic Coulomb stress change from the 1992 M7.3 Landers, California, earthquake and the hypocenter of the 1999 M7.1 Hector Mine, California earthquake. *J Geophys Res* 108:2012.
2. Freed AM (2005) Earthquake triggering by static, dynamic, and postseismic stress transfer. *Annu Rev Earth Planet Sci* 33:335–367.
3. Felzer KR, Brodsky EE (2005) Testing the stress shadow hypothesis. *J Geophys Res* 110:B05S09.
4. Gomberg J, Johnson P (2005) Dynamic triggering of earthquakes. *Nature* 437:830.
5. Felzer KR, Brodsky EE (2006) Decay of aftershock density with distance indicates triggering by dynamic stress. *Nature* 441:735–738.
6. Richards-Dinger K, Stein RS, Toda S (2010) Decay of aftershock density with distance does not indicate triggering by dynamic stress. *Nature* 467:583–586.
7. Velasco AA, Hernandez S, Parsons T, Pankow K (2008) Global ubiquity of dynamic earthquake triggering. *Nature Geoscience* 1:375–379.
8. Parsons T, Velasco AA (2011) Absence of remotely triggered large earthquakes beyond the mainshock region. *Nature Geoscience* 4:312–316.
9. Chlieh M, et al. (2007) Coseismic slip and afterslip of the great Mw 9.15 Sumatra—Andaman earthquake of 2004. *Bull Seismol Soc Am* 97:S152–S173.
10. Banerjee P, Pollitz F, Nagrajan B, Burgmann R (2007) Coseismic slip distributions of the 26 December 2004 Sumatra–Andaman and 28 March Nias earthquakes from GPS static offsets. *Bull Seismol Soc Am* 97:S86–S102.
11. Shearer P, Bürgmann R (2010) Lessons learned from the 2004 Sumatra-Andaman Megathrust Rupture. *Ann Rev Earth Planet Sci* 38:103–131.
12. Curray JR (2005) Tectonics and history of the Andaman Sea region. *J Asian Earth Sci* 25:187–232.
13. McCaffrey R (2009) The tectonic framework of the Sumatran subduction zone. *Annu Rev Earth Planet Sci* 37:345–366.
14. Cochran JR (2010) Morphology and tectonics of the Andaman Forearc, northeastern Indian Ocean. *Geophys J Int* 182:631–651.
15. Stein RS (1999) The role of stress transfer in earthquake occurrence. *Nature* 402:605–609.
16. Pesicek JD, et al. (2010) Teleseismic double-difference relocation of earthquakes along the Sumatra-Andaman subduction zone using a 3-D model. *J Geophys Res* 115:B10303.
17. Gardner KK, Knopoff L (1974) Is the sequence of earthquakes in southern California, with aftershocks removed, Poissonian? *Bull Seismol Soc Am* 64:1363–1367.
18. Andrade V, Rajendran K (2011) Intraplate response to the Great 2004 Sumatra–Andaman earthquake: A study from the Andaman segment. *Bull Seismol Soc Am* 101:506–514.
19. Buck WR, Lavier LL, Poliakov ANB (2005) Modes of faulting at mid-ocean ridges. *Nature* 434:719–723.
20. Rubin AM, Pollard DD (1988) Dike-induced faulting in rift zones of Iceland and Afar. *Geology* 16:413–417.
21. Dziewonski AM, Anderson DL (1981) Preliminary reference Earth model. *Phys Earth and Planet Int* 25:297–356.
22. Friederich W, Dalkolmo J (1995) Complete synthetic seismograms for a spherically symmetric earth by a numerical computation of the Green's function in the frequency domain. *Geophys J Int* 122:537–550.
23. Pollitz FF, Rubinstein JL, Ellsworth WL (2012) Source characterization of near-surface chemical explosions at SAFOD. *Bull Seismol Soc Am* 102, in press.
24. Ishii M, Shearer PM, Houston H, Vidale JE (2005) Extent, duration and speed of the 2004 Sumatra–Andaman earthquake imaged by the Hi-Net array. *Nature* 435:933–936.
25. Brodsky EE, Prejean SG (2005) New constraints on mechanisms of remotely triggered seismicity at Long Valley Caldera. *J Geophys Res* 110:B04302.
26. Zoback MD, et al. (1987) New evidence on the state of stress of the San Andreas fault system. *Science* 238:1105–1111.
27. Parsons T, Stein RS, Simpson RW, Reasenberg PA (1999) Stress sensitivity of fault seismicity: A comparison between limited-offset oblique and major strike-slip faults. *J Geophys Res* 104:20183–20202.
28. Floyd JS, Tolstoy M, Mutter JC, Scholz CH (2002) Seismotectonics of mid-ocean ridge propagation in Hess Deep. *Science* 298:1765–1768.
29. Arnadottir T, Jonsson S, Pedersen R, Gudmundsson GB (2003) Coulomb stress changes in the South Iceland Seismic Zone due to two large earthquakes in June 2000. *Geophys Res Letts* 30:1205.
30. Hardebeck JL, Nazareth JJ, Hauksson E (1998) The static stress change triggering model: Constraints from two southern California aftershocks sequences. *J Geophys Res* 103:24427–24437.
31. Mallman EP, Parsons T (2008) A Global search for stress shadows. *J Geophys Res* 113:B12304.
32. Toda S, Stein RS, Beroza GC, Marsan D (2012) Aftershocks halted by static stress shadows. *Nature Geoscience* 5:410–413, 10.1038/ngeo1465.
33. Toda S, Stein RS, Lin J (2011) Widespread seismicity excitation throughout central Japan following the 2011 $M = 9.0$ Tohoku earthquake, and its interpretation by Coulomb stress transfer. *Geophys Res Lett* 38:L00G03.
34. Cattin R, et al. (2009) Stress change and effective friction coefficient along the Sumatra-Andaman-Sagaing fault system after the 26 December 2004 (Mw = 92) and the 28 March 2005 (Mw = 8.7) earthquakes. *Geochem Geophys Geosys Geosys* 10:Q03011.
35. Raju KAK, Ramprasad T, Rao PS, Rao BR, Varghese J (2004) New insights into the tectonic evolution of the Andaman basin, northeast Indian Ocean. *Earth Planet Sci Letts* 221:145–162.
36. Engdahl ER, Villasenor A, DeShon HR, Thurber CH (2007) Teleseismic relocation and assessment of seismicity (1918–2005) in the region of the 2004 Mw 9.0 Sumatra–Andaman and 2005 Mw 8.6 Nias Island great earthquakes. *Bull Seismol Soc Am* 97:S43–S61.
37. Boore D (2011) *Earthquake Data in Engineering Seismology: Predictive Models, Data Management, and Networks*, eds S Akkar, P Gülkan, and TV Eck (Springer, Dordrecht), pp 3–15.
38. Gledhill K, Ristau J, Reyners M, Fry B, Holden C (2011) The Darfield (Canterbury, New Zealand) Mw 7.1 earthquake of September 2010: A preliminary seismological report. *Seismol Res Letts* 82:378–386.
39. Muir-Wood R (2012) Risk and Insurance Research: Extreme events and insurance. (The Geneva Association, Geneva), 93 p 106.
40. Genrich JF, et al. (2000) Distribution of slip at the northern Sumatra fault system. *J Geophys Res* 105:28327–28341.

Supporting Information

Sevilgen et al. 10.1073/pnas.1208799109

SI Text

Details of the Dynamic Coulomb Stress Model. Our simulations in a spherically-symmetric structure account for first-order directivity effects and geometrical and intrinsic attenuation (evident in Movie S1), but do not incorporate wave propagation through laterally heterogeneous media (1). The latter would include lateral refraction, focusing and de-focusing, and multiple scattering, e.g., basin reverberations and amplification. We regard these effects as important locally but of second order for the understanding for the character of the regional wave propagation and amplitude of time-dependent dynamic stress at the receiver faults. Earth's sphericity becomes important in the phase arrival times over the 1500 km distance between the epicenter and the northern backarc. A limitation of our stressgrams is their 6 s (0.17 Hz) minimum period, but at the 200–400 km distances from the source that we consider, such short period energy is already attenuated.

We generate synthetic seismograms using the Direct Green's Function (DGF) method (2). This synthesizes the seismic wave field for a spherically layered structure of seismic velocities Vp and Vs, density, and attenuation factors Qp and Qs in the l-Ω domain, where l denotes spherical harmonic degree. It is the spherical equivalent of the frequency-wave number method employed for flat-layered structures (3). It has been validated against analytic solutions, including those for elastic wave propagation in a full space for both isotropic and shear sources [eqn 4.29 of (4)], in a half-space the independent numerical solutions AXITRA (5) and f-k method (3), and in a layered spherical geometry the axisymmetric spectral-element code AXISEM (6).

Alternative approaches to calculating the dynamic Coulomb stresses include that of Cotton and Coutant (7), which uses a discrete wavenumber reflectivity method to compute the stress field radiated by arbitrary moment-tensor sources in plane-layered media. From the expressions giving the potentials radiated by single forces (5), they derived the upward and downward potentials in the source layers. Their code has been widely used (8–14). Karabulut et al. (15) used the method of Bouchon (5). Doser et al. (1) used the code of Olsen (16), a fourth-order finite-difference method, in which 3D basin velocity structure was included.

1. Doser DI, Olsen KB, Pollitz FF, Stein RS, Toda S (2009) The 1911 $M \sim 6.6$ Calaveras earthquake: Source arameters and the role of static, viscoelastic and dynamic Coulomb stress changes imparted by the 1906 San Francisco earthquake. *Bull Seismol Soc Amer* 99:1746–1759.
2. Friederich W, Dalkolmo J (1995) Complete synthetic seismograms for a spherically symmetric earth by a numerical computation of the Green's function in the frequency domain. *Geophys J Int* 122:537–550.
3. Zhu L, Rivera LA (2002) A note on the dynamic and static displacements from a point source in multilayered media. *Geophys J Int* 148:619–627.
4. Aki K, Richards PG (1980) *Quantitative Seismology* (W.H. Freeman & Co., New York).
5. Bouchon M (1981) A simple method to calculate greens functions for elastic layered media. *Bull Seismol Soc Am* 71:959–971.
6. Nissen-Meyer T, Fournier A, Dahlen FA (2007) A two-dimensional spectral-element method for spherical-earth seismograms, I. Moment-tensor source. *Geophys J Int* 148:1067–1092.
7. Cotton F, Coutant O (1997) Dynamic stress variations due to shear faults in a plane-layered medium. *Geophys J Int* 128:676–688.
8. Gomberg J (1996) Stress/strain changes and triggered seismicity following the Mw7.3 Landers, California, earthquake. *J Geophys Res* 101:751–764.
9. Gomberg J, Beeler NM, Blanpied ML, Bodin P (1998) Earthquake triggering by transient and static deformations. *J Geophys Res* 103:24411–24426.
10. Kilb D, Gomberg J, Bodin P (2000) Earthquake triggering by dynamic stresses. *Nature* 408:570–574.
11. Kilb D (2003) A strong correlation between induced peak dynamic Coulomb stress change from the 1992 M7.3 Landers, California, earthquake and the hypocenter of the 1999 M7.1 Hector Mine, California earthquake. *J Geophys Res* 108:2012.
12. Gomberg J, Johnson P (2005) Dynamic triggering of earthquakes. *Nature* 437:830.
13. Antonioli A, Belardinelli ME, Bizzarri A, Vogfjord KS (2006) Evidence of instantaneous dynamic triggering during the seismic sequence of year 2000 in south Iceland. *J Geophys Res* 111:B03302.
14. Gomberg J, Felzer KR (2008) A model of earthquake triggering probabilities and application to dynamic deformations constrained by ground motion observations. *J Geophys Res* 113:B10317.
15. Karabulut H, et al. (2011) Evolution of the seismicity in the eastern Marmara Sea a decade before and after the 17 August 1999 Izmit earthquake. *Tectonophysics* 510:17–27.
16. Olsen KB (1994) Simulation of three-dimensional wave propagation in the Salt Lake Basin. (PhD thesis thesis, Univ Utah).

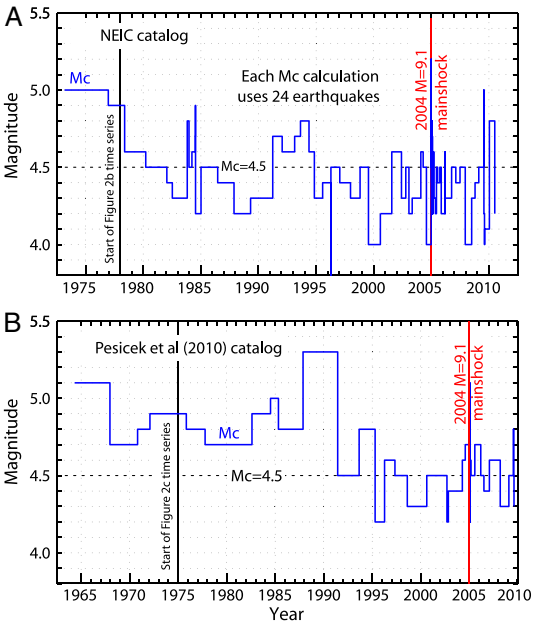

Fig. S1. Magnitude of completeness as a function of time. We calculated the magnitude of completeness, Mc, for successive bins of 24 earthquakes, rather than successive uniform time-periods, in the Sumatra-Andaman back-arc over 93°–97° lon., 6.9°–17.0° lat. by least squares. (*A*) The NEIC catalog from 3/7/1973 to 7/12/2011. (*B*) The relocated (1) catalog from 5/1/1964 to 9/5/2009 (the end of this catalog).

1 Pesicek JD et al (2010) Teleseismic double-difference relocation of earthquakes along the Sumatra-Andaman subduction zone using a 3-D model. *J Geophys Res* 115:B10303.

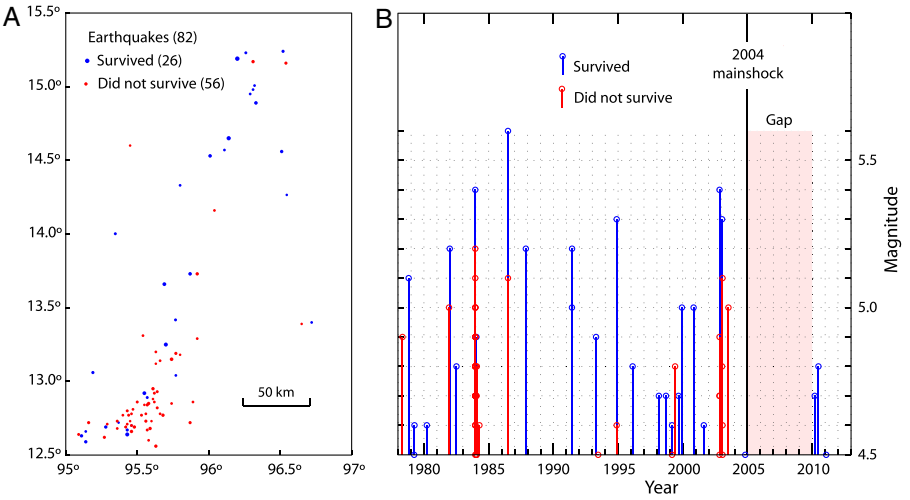

Fig. S2. Comparison of the full and declustered catalog along the backarc-transform system. We declustered the NEIC catalog using the algorithm by reference (1) for Mc ~ 4.5. (*A*) Map view. Blue dots represent surviving (declustered) earthquakes; green dots represent earthquakes that did not survive. (*B*) Time series. Blue stems represent surviving earthquakes; black stems represent the full catalog.

1 Gardner KK, Knopoff L (1974) Is the sequence of earthquakes in southern California, with aftershocks removed, Poissonian? *Bull Seismol Soc Am* 64:1363–1367.

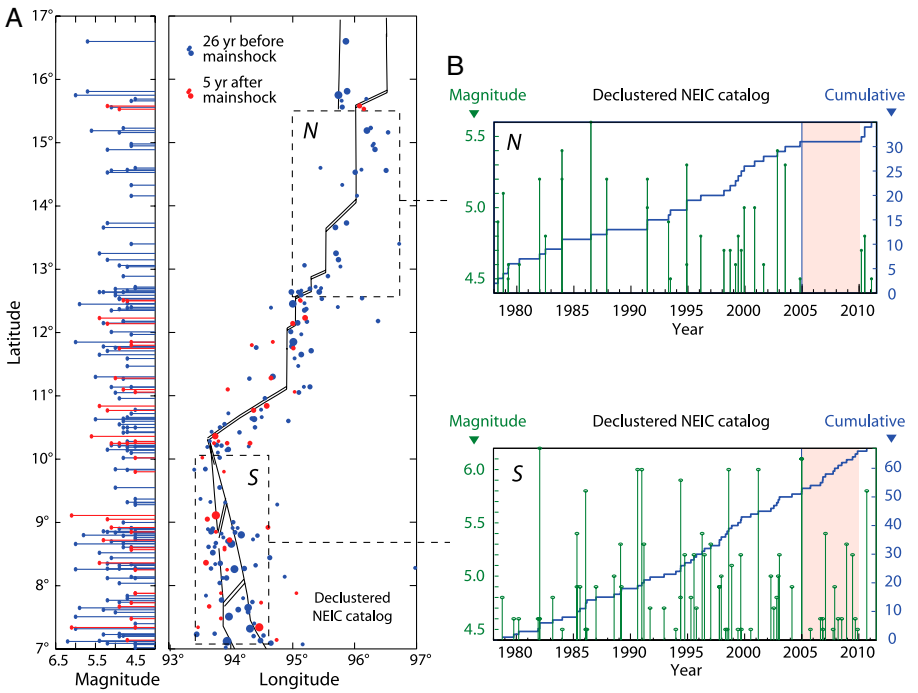

Fig. S3. Map (*A*) and time series (*B*) of the declustered catalog (1), which can be compared to Figs. 2 *A*, *B* and 3.

1 Gardner KK, Knopoff L (1974) Is the sequence of earthquakes in southern California, with aftershocks removed, Poissonian? *Bull Seismol Soc Am* 64:1363–1367.

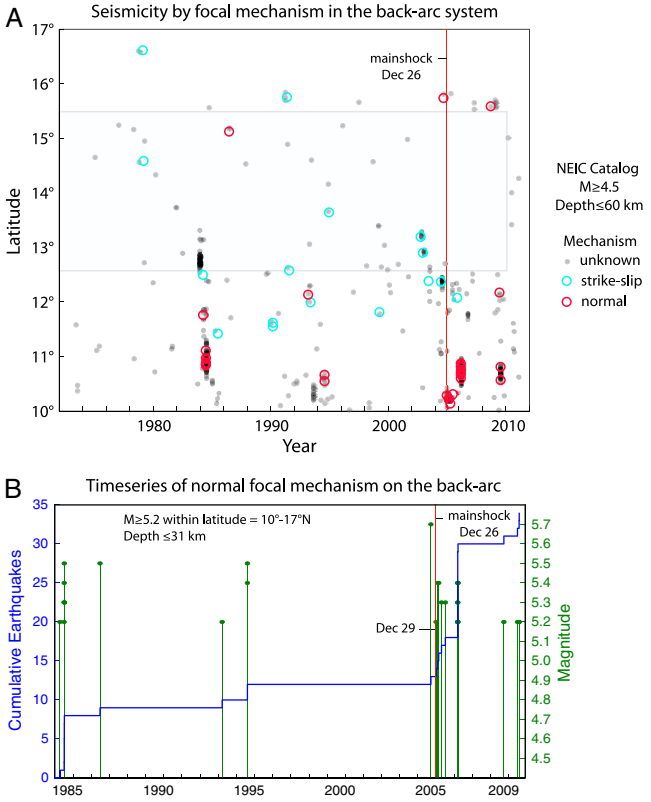

Fig. S4. Time series of earthquakes by focal mechanism. (*A*) The shutdown area at 12.5–15.5 °N lat. was characterized by strike-slip events before the 2004 mainshocks, whereas the activation area at 10–11.5 °N lat. was characterized by normal events both before and after the mainshock. (*B*) Rift mechanisms in the Andaman backarc show an increased rate after the 2004 mainshock, but no events triggered during the passage of the surface waves.

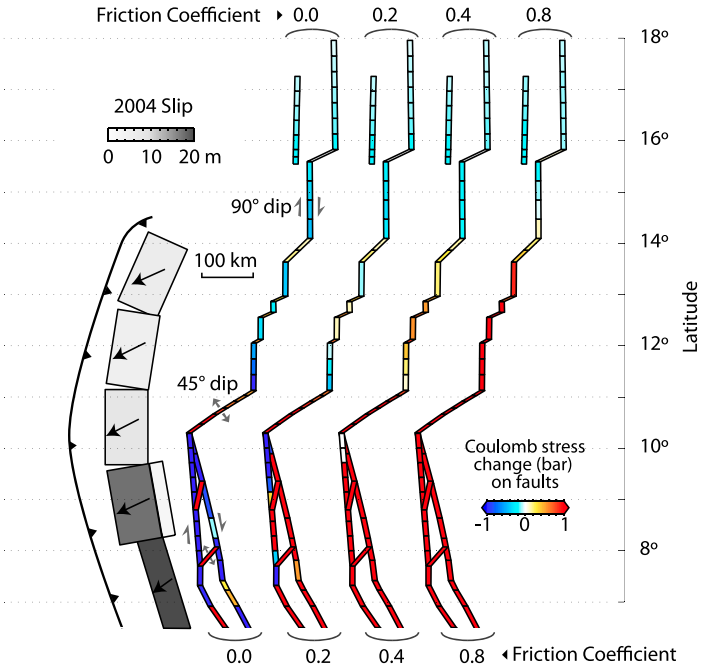

Fig. S5. Coulomb stress at 10 km depth as a function of friction on the back-arc system by imparted the 2004 mainshock, using the 8-patch (1) source model. Results are similar to that for Fig. 8, but favor a slightly lower friction to match the earthquake observations south of 14 °N lat.

1 Banerjee P, Pollitz F, Nagrajan B, Burgmann R (2007) Coseismic slip distributions of the 26 December 2004 Sumatra–Andaman and 28 March Nias earthquakes from GPS static offsets. *Bull Seismol Soc Am* 97:S86–S102.

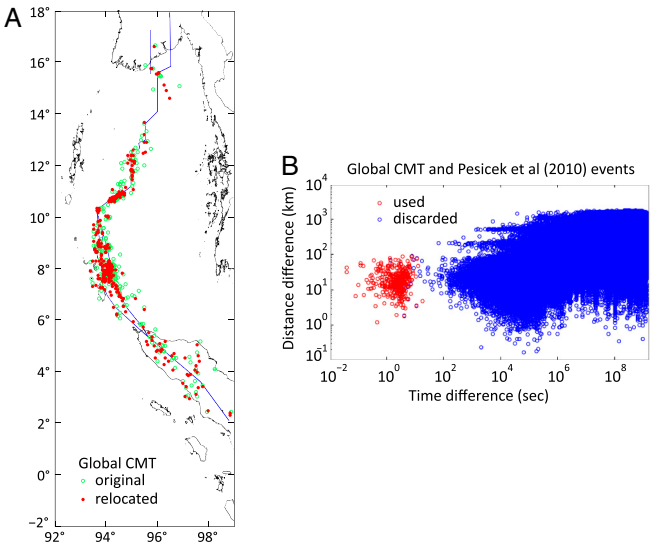

Fig. S6. Relocating Global CMT earthquakes. The gCMT events associated with their relocated equivalents in (1) along the backarc (*A*). We obtained 376 relocations; 4 gCMT events were not relocatable. Most matched events occur within 2 sec and 30 km of each other; all are $M \geq 5.2$ (*B*). Earthquake origin time was used as the sole association criteria; this resulted in relocations of 1–100 km.

1 Pesicek JD et al (2010) Teleseismic double-difference relocation of earthquakes along the Sumatra-Andaman subduction zone using a 3-D model. *J Geophys Res* 115:B10303.

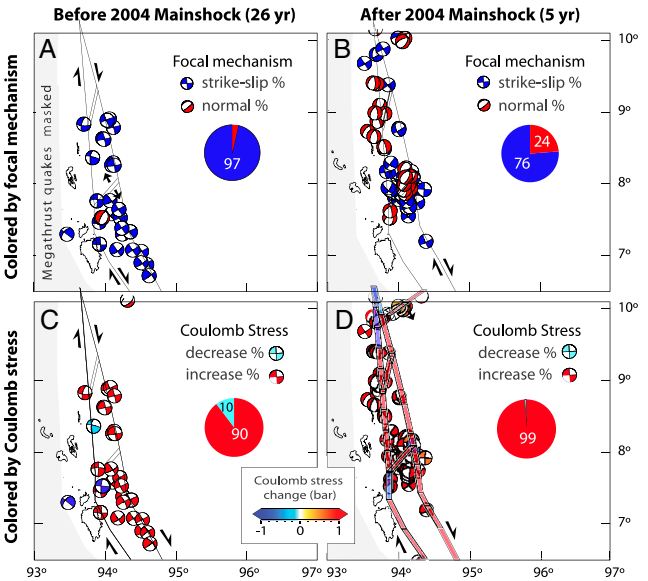

Fig. S7. Activation of rift events south of 10° lat. imparted by the 2004 mainshock. We relocated gCMT earthquakes from Box S of Fig. 2 so that they could be associated with the back-arc-transform system (Fig. S6). (*A*–*B*) Earthquakes are colored by focal mechanism; (*C*–*D*) earthquakes are colored by the Coulomb stress change from the 2004 mainshock (1) using the most-northerly striking nodal planes as the receivers and friction of 0.4; (*A*–*C*) Earthquakes occurring before the 2004 mainshock; (*B*–*D*) Earthquakes occurred after the mainshock. This rate increase was previously reported (2–4). Although these earthquakes are close to the 2004 rupture surface and so more sensitive to the nearby megathrust slip distribution, they, too, show a change in focal mechanisms after the 2004 earthquake (*A*–*B*): whereas only 3% of the events were strike-slip before the mainshock, 24% were afterwards. Although 99% of the post-2004 mechanisms are calculated to be promoted by the 2004 earthquake, 90% were so beforehand (*C*–*D*), yielding a 110% gain in promoted mechanisms.

1 Chlieh M et al (2007) Coseismic slip and afterslip of the great Mw 9.15 Sumatra–Andaman earthquake of 2004. *Bull Seismol Soc Am* 97:S152–S173.

2 Zhu L, Rivera L A(2002), A note on the dynamic and static displacements from a point source in multilayered media. *Geophys J Int* 148: 619–627.

3 Cattin R et al (2009) Stress change and effective friction coefficient along the Sumatra-Andaman-Sagaing fault system after the 26 December 2004 (Mw=9.2) and the 28 March 2005 (Mw=8.7) earthquakes. *Geochem Geophys Geosys Geosys*10:Q03011.

4 Raju KAK, Ramprasad T, Rao PS, Rao BR, Varghese J (2004) New insights into the tectonic evolution of the Andaman basin, northeast Indian Ocean. *Earth Planet Sci Letts* 221:145–162.

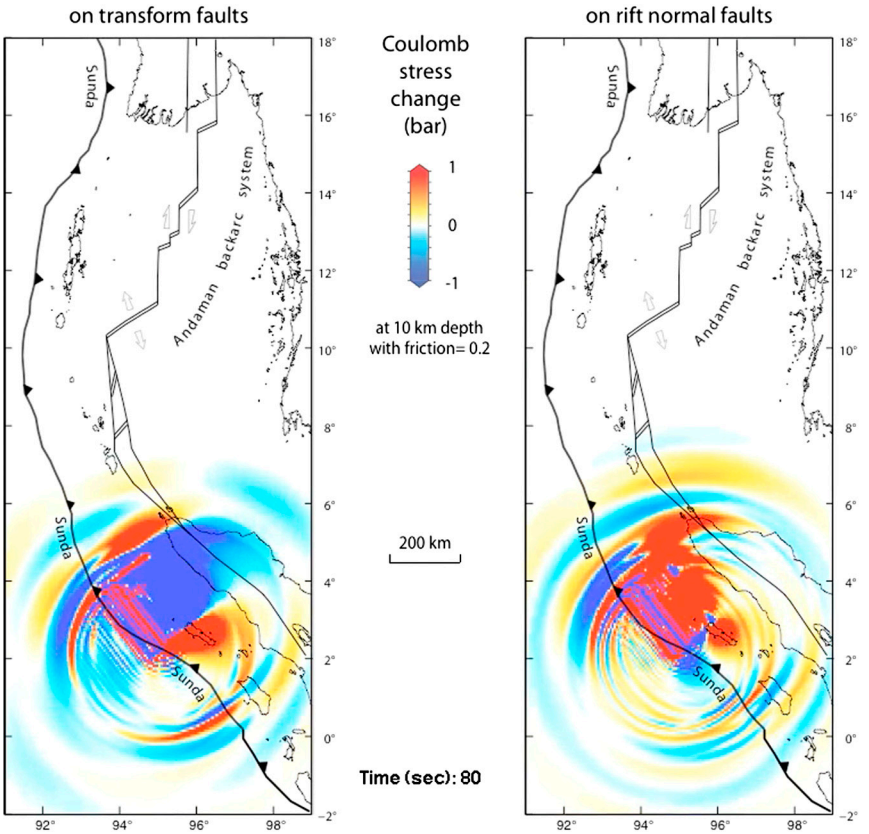

Movie S1. (1 min 22 s duration; example frame is shown.) First, the seismicity before and after the 2004 $M = 9.2$ Sumatra earthquake is shown in map view and time series. Then, the dynamic Coulomb stress is shown at 10 km depth using the Banerjee (1) source rupturing northward at 2.8 km/s (2). The left panel resolves the stress on N-striking vertical right-lateral transform faults; the right panel resolves stress on N45 °E-striking normal faults dipping 45 °SE typical of the rift sections. The movie covers the first 1000 s after earthquake nucleation, and plays at about 20 times faster than real time.

Movie S1 (MP4)

1 Banerjee P, Pollitz F, Nagrajan B, Burgmann R (2007) Coseismic slip distributions of the 26 December 2004 Sumatra–Andaman and 28 March Nias earthquakes from GPS static offsets. *Bull Seismol Soc Amer* 97:S86–S102.
2 Ishii M, Shearer PM, Houston H, Vidale JE (2005) Extent, duration and speed of the 2004 Sumatra–Andaman earthquake imaged by the Hi-Net array. *Nature* 435:933–936.

Table S1. Focal mechanism rate and stress change (2005–2010 relative to 1975–2004) in the region of Fig. 3

	Number of $M \geq 5.2$ mechanisms		
Focal mechanism	Before mainshock	After mainshock	Rate change
Strike-slip	15	1	0.34
Normal	13	20	8.00

Rate change = rate after mainshock/rate before mainshock.

	Mainshock			
Focal mechanism	Before	After	Gain in promoted earthquakes	Significance
Promoted/All	15/23	20/20	53%	0.03%

Gain = (ratio after mainshock/ratio before mainshock)$^{-1}$.